RSC Advances

PAPER

View Article Online
View Journal | View Issue

Cite this: *RSC Adv.*, 2022, **12**, 28720

Organic–inorganic hybrid $[NH_3(CH_2)_6NH_3]ZnBr_4$ crystal: structural characterization, phase transitions, thermal properties, and structural dynamics†

Ae Ran Lim *[ab] and Huiyeong Ju[c]

Organic–inorganic hybrid $[NH_3(CH_2)_6NH_3]ZnBr_4$ crystals were prepared by slow evaporation; the crystals had a monoclinic structure with space group $P2_1/c$ and lattice constants a = 7.7833 Å, b = 14.5312 Å, c = 13.2396 Å, β = 90.8650°, and Z = 4. They underwent two phase transitions, at 370 K (T_{C1}) and 430 K (T_{C2}), as confirmed by powder X-ray diffraction patterns at various temperatures; the crystals were stable up to 600 K. The nuclear magnetic resonance spectra, obtained using the magic-angle spinning method, demonstrated changes in the ^{1}H and ^{13}C chemical shifts were observed near T_{C1}, indicating changing structural environments around ^{1}H and ^{13}C. The spin–lattice relaxation time, $T_{1\rho}$, increased rapidly near T_{C1} suggesting very large energy transfer, as indicated by a large thermal displacement around the ^{13}C atoms of the cation. However, the environments of ^{1}H, ^{14}N, and C1 located close to NH_3 in the $[NH_3(CH_2)_6NH_3]$ cation did not influence it significantly, indicating a minor change in the N–H···Br hydrogen bond with the coordination geometry of the $ZnBr_4$ anion. We believe that the information on the physiochemical properties and thermal stability of $[NH_3(CH_2)_6NH_3]ZnBr_4$, as discussed in this study, would be key to exploring its application in stable, environment friendly solar cells.

Received 3rd August 2022
Accepted 30th September 2022

DOI: 10.1039/d2ra04834e

rsc.li/rsc-advances

1. Introduction

Solar cells based on organic–inorganic hybrid materials have been extensively studied. Typically, $CH_3NH_3PbX_3$ (X = Cl, Br, and I) thin-film photovoltaic devices have been used as solar cells;[1–6] however, these substances readily decompose in humid air and are toxic because of the presence of Pb. Therefore, it is necessary to develop eco-friendly hybrid perovskite solar cells. Recently, a new series of perovskite compounds $[(CH_3)_2NH_2]Zn(HCOO)_3$, consisting of an organic cation and a metal ion bridged by formate ions, has been reported.[7–13] They have the potential for application in novel memory storage and manipulation devices. In addition, research on type of organic–inorganic hybrid perovskites $[NH_3(CH_2)_nNH_3]BX_4$ (n = 2, 3, 4, …; B = Mn, Co, Cu, Zn, Cd; X = Cl, Br, I), with a focus on the optimization of the perovskite structure and dynamics investigation, is rapidly garnering attention. The physical properties of organic–inorganic hybrids depend on their organic cations, inorganic anion coordination geometry of the metal ions (BX_4^{2-} or BX_6^{2-}), and halogen ions.[14–24] The organic cations of hybrid perovskites induce structural flexibility and nonlinear optical properties, whereas the inorganic anion is attributable for thermal and mechanical properties.[25,26] The crystal structures with B = Mn, Cu, and Cd consist of alternate octahedrons, $(BX_6)^{2-}$, and organic chains, and is two-dimensional structure. The ammonium ion of the organic group is connected by a N–H···X hydrogen bond to the halide ion of the inorganic layer, rendering such structures good candidates for proton conduction.[16] The isolated tetrahedral structures with B = Co and Zn are formed, where an inorganic layer of $(BX_4)^{2-}$ is sandwiched between the organic cation, and zero-dimensional structure.[18,27–29] The crystal consists of unassociated tetrahedrally distorted $(BX_4)^{2-}$ anions and cations linked by H bonds to X^- ions. Structural rearrangements due to conformational changes in the chains are important for long-chain alkylenediammonium materials $[NH_3(CH_2)_nNH_3]BX_4$, with n >> 4.[30] Among them, the organic–inorganic perovskite type $[NH_3(CH_2)_6NH_3]ZnBr_4$ (1, 6-hexanediammonium tetrabromozincate(II)), containing $[NH_3(CH_2)_6NH_3]$ cations and layered $ZnBr_4$ anions (with Zn atoms surrounded by four Br atoms to form the $ZnBr_4$ tetrahedron), is an interesting hybrid material.

Ishiha and Horiuchi[31] measured the ^{81}Br nuclear quadrupole resonance (NQR) frequencies of $[NH_3(CH_2)_6NH_3]ZnBr_4$ below

[a]*Graduate School of Carbon Convergence Engineering, Jeonju University, Jeonju 55069, Korea*

[b]*Department of Science Education, Jeonju University, Jeonju 55069, Korea. E-mail: aeranlim@hanmail.net; arlim@jj.ac.kr*

[c]*Korea Basic Science Institute, Seoul Western Center, Seoul 03759, Korea*

† Electronic supplementary information (ESI) available: XRD data, bond distances and angles, and hydrogen-bond geometrics of the crystal structure. CCDC 2169730. For ESI and crystallographic data in CIF or other electronic format see DOI: https://doi.org/10.1039/d2ra04834e

room temperature. Four resonance signals were assigned to the four bromine atoms in the tetrahedron. The N–H···Br hydrogen bonds between the cations and anions were considered based on these temperature dependences. In addition, the phase transition temperature, measured by differential scanning calorimetry (DSC), was not observed below room temperature, but was observed at 380 K and 424 K above room temperature; the melting point was 475 K.[31] The crystal structure and electronic properties of $[NH_3(CH_2)_6NH_3]ZnCl_4$ similar to the $[NH_3(CH_6)NH_3]ZnBr_4$ crystal were reported by Mostafa and Elkhiyami.[16] Although the NQR data and phase transition temperatures have been reported, to the best of our knowledge, investigation of crystal structure, thermodynamic stability and structural dynamics with respect to temperature change has not been widely conducted.

This study is the first to investigate the crystal structures, phase transition temperature (T_C), and thermodynamic properties of $[NH_3(CH_2)_6NH_3]ZnBr_4$ crystals with zero-dimensional. Secondly, nuclear magnetic resonance (NMR) chemical shifts and spin–lattice relaxation times ($T_{1\rho}$) for ^1H and ^{13}C were also measured to understand the coordination geometry and molecular dynamics of the organic $[NH_3(CH_2)_6NH_3]$ cation near T_C. In addition, the effect of temperature on the static ^{14}N NMR spectra was investigated to elucidate the atomic configurations of the cation. The change in the coordination geometry in response to temperature change was explained by the changes of N–H···Br hydrogen bonds between the cations and tetrahedral $ZnBr_4$ anions. The investigation of the crystal structures and physicochemical properties of the phase transition mechanism conducted herein will expand the application scope of $[NH_3(CH_2)_6NH_3]ZnBr_4$ crystals in environmentally friendly solar cells.

2. Experimental

To obtain $[NH_3(CH_2)_6NH_3]ZnBr_4$ single crystals, an aqueous solution containing $NH_2(CH_2)_6NH_2 \cdot 2HBr$ (Aldrich, USA) and $ZnBr_2$ (Aldrich, 99.99%, USA) in 1 : 1 ratio was slowly evaporated in a thermostat at 300 K. Colorless single crystals ($10 \times 3 \times 2$ mm) were grown for approximately five weeks. The single crystal grown here was colorless and transparent, with a long rectangular shape.

Fourier transformation infrared (FT-IR) spectra in the 4000–500 cm^{-1} range were measured using an FT-IR spectrometer (PerkinElmer, L1600300) with a compressed KBr pellet.

The lattice parameters at various temperatures were determined by single-crystal X-ray diffraction (XRD) at the Seoul Western Center of the Korea Basic Science Institute (KBSI). A colorless crystal block was picked up with paratone oil and mounted on a Bruker D8 Venture PHOTON III M14 diffractometer equipped with a graphite-monochromated Mo-Kα (λ = 0.71073 Å) radiation source and a nitrogen cold stream (−50 °C). Data was collected and integrated using SMART APEX3 (Bruker, 2016) and SAINT (Bruker, 2016). The absorption was corrected by a multi-scan method implemented in SADABS. The structure was solved using direct methods and refined by full-matrix least-squares on F^2 using SHELXTL.[32] All non-hydrogen atoms were refined anisotropically, and the hydrogen atoms were added to their geometrically ideal positions. Additionally the powder XRD patterns of the $[NH_3(CH_2)_6NH_3]ZnBr_4$ crystals were measured at several temperatures using an XRD system with a Mo-Kα radiation source.

The DSC experiments were performed using a DSC 25 apparatus (TA Instruments, USA) at heating and cooling rates of 10 K min^{-1} from 200 to 570 K in a nitrogen gas atmosphere.

Thermogravimetric analysis (TGA) and differential thermal analysis (DTA) experiments were performed on a thermogravimetric analyzer (TA Instruments, USA) at the heating rate identical to that utilized for DSC at 300–873 K under nitrogen gas.

The NMR chemical shifts of the $[NH_3(CH_2)_6NH_3]ZnBr_4$ crystals were measured using a Bruker 400 MHz Avance II+ NMR spectrometer (Bruker, Germany) at KBSI. The Larmor frequency for ^1H magic-angle spinning (MAS) NMR was $\omega_o/2\pi$ = 400.13 MHz, and that for the ^{13}C MAS NMR experiment was $\omega_o/2\pi$ = 100.61 MHz. To minimize spinning sidebands, the MAS speeds for ^1H and ^{13}C were measured at 5 kHz. Tetramethylsilane (TMS) was used as a reference material for accurate NMR chemical shift measurements. The spin–lattice relaxation time, $T_{1\rho}$, values were obtained using a $\pi/2$–τ pulse, followed by a spin-lock pulse of duration τ, and the $\pi/2$ pulse widths for ^1H and ^{13}C were measured by a previously published method.[33] Static ^{14}N NMR resonance frequencies were recorded with a Larmor frequency of $\omega_o/2\pi$ = 28.90 MHz using the one-pulse method and NH_4NO_3 was used as the reference material. The temperature during the NMR experiment ranged from 180 to 430 K; owing to the limitations of the instrument, measurements at higher temperatures were not possible.

3. Results and discussion

3.1. FT-IR spectra

The FT-IR spectrum within the 4000–500 cm^{-1} range was recorded at room temperature. The result is shown in Fig. 1, and

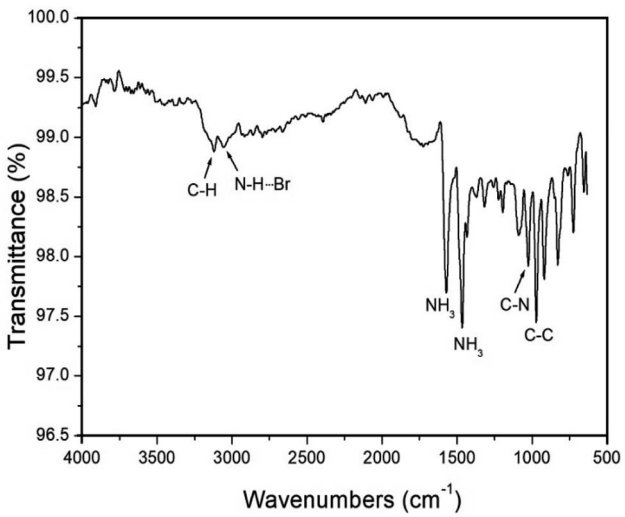

Fig. 1 FT-IR spectrum of $[NH_3(CH_2)_6NH_3]ZnBr_4$ at room temperature.

the peak near 3128 cm^{-1} is assigned to the C–H mode. And, the peak at 3058 cm^{-1} is due to the N–H···Br hydrogen bond, and those at 1577 and 1469 cm^{-1} correspond to the asymmetric deformation of NH_3 and symmetric deformation of NH_3, respectively. The peaks near 1025 and 973 cm^{-1} are defined to the C–N and C–C mode.

3.2. Crystal structure and phase transition

Single-crystal XRD patterns for $[NH_3(CH_2)_6NH_3]ZnBr_4$ crystals were obtained at several temperatures. At 300 K, the hybrid was found to have crystallized as a monoclinic system with a $P2_1/c$ space group and had lattice constants a = 7.7833 (2) Å, b = 14.5312 (4) Å, c = 13.2396 (3) Å, β = 90.8650 (1)°, and Z = 1. Table 1 lists single-crystal XRD and refinement data of the $[NH_3(CH_2)_6NH_3]ZnBr_4$ crystal, and Fig. 2 shows its structure. The atomic numbering scheme and thermal ellipsoids for the H atoms are shown in Fig. 3, and their bond lengths and angles are summarized in Table 2. The Zn atom is coordinated by four Br atoms, forming a nearly regular tetrahedron of $ZnBr_4$. The hydrogen atoms of each formula unit are able to form hydrogen bonds N–H···Br. The changes in the lattice parameters at 230, 250, 270, 300, and 350 K are shown in Fig. 4, where a, b, and c

Table 1 Crystal data and structure refinement for $[NH_3(CH_2)_6NH_3]ZnBr_4$ at 300 K. The full data are available in the CIF files

Chemical formula	$C_6H_{18}N_2ZnBr_4$
Weight	503.23
Crystal system	Monoclinic
Space group	$P2_1/c$
T (K)	300
a (Å)	7.7833
b (Å)	14.5312
c (Å)	13.2396
β (°)	90.8650(10)
Z	4
V (Å^3)	1497.24
Radiation type	Mo-Kα
Wavelength (Å)	1.71073
Reflections collected	27 490
Independent reflections	3572 (R_{int} = 0.0452)
Goodness-of-fit on F^2	1.047
Final R indices [I > 2sigma(I)]	R_1 = 0.0300, wR_2 = 0.0633
R indices (all data)	R_1 = 0.0421, wR_2 = 0.0677

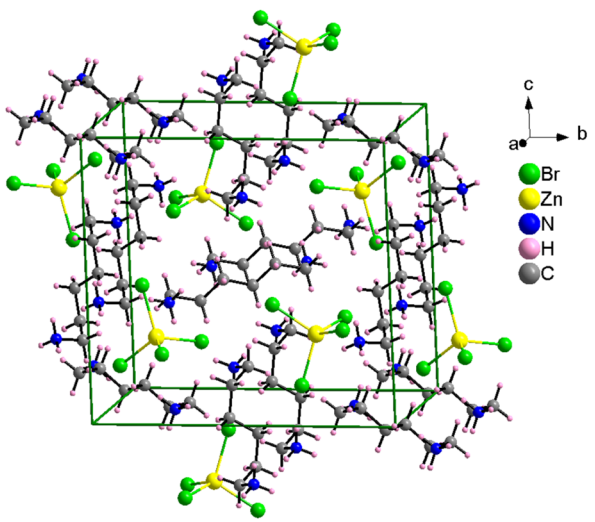

Fig. 2 Crystal structure of $[NH_3(CH_2)_6NH_3]ZnBr_4$ at 300 K.

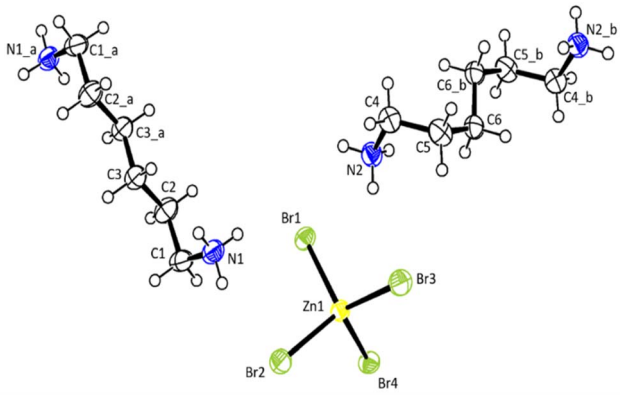

Fig. 3 Thermal ellipsoid plot (50% probability) for structure of $[NH_3(CH_2)_6NH_3]ZnBr_4$.

Table 2 Bond-lengths (Å) and bond-angles (°) at 300 K

Bond-length (Å) and bond-angle (°)			
Br(1)–Zn(1)	2.4139 (5)	Br(3)–Zn(1)–Br(1)	110.07 (2)
Br(2)–Zn(1)	2.4333 (5)	Br(3)–Zn(1)–Br(4)	111.31 (2)
Br(3)–Zn(1)	2.3822 (6)	Br(1)–Zn(1)–Br(4)	108.08 (2)
Br(4)–Zn(1)	2.4264 (5)	Br(3)–Zn(1)–Br(2)	112.00 (2)
		Br(1)–Zn(1)–Br(2)	107.482 (19)
		Br(4)–Zn(1)–Br(2)	107.73 (2)
N(1)–C(1)	1.487 (5)		
C(1)–C(2)	1.523 (5)		
C(2)–C(3)	1.522 (5)		
C(3)–C(3)	1.507 (7)		

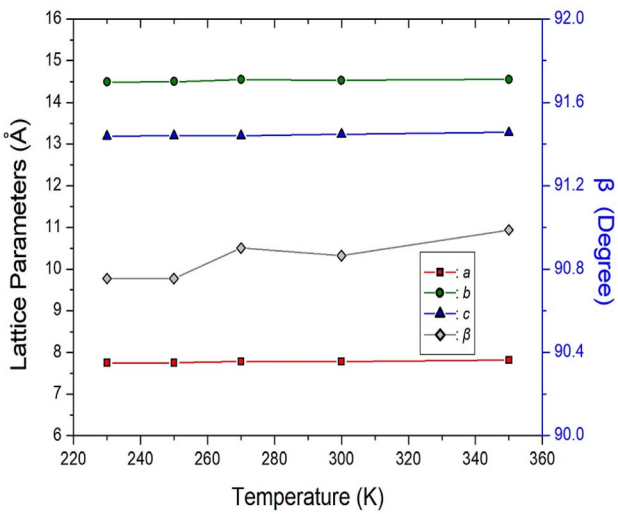

Fig. 4 The lattice parameters a, b, c, and β of $[NH_3(CH_2)_6NH_3]ZnBr_4$ crystal according to the temperatures.

have different thermal expansion upon with increasing temperature and β increases slightly with increasing temperature.

The DSC analysis was performed on the $[NH_3(CH_2)_6NH_3]ZnBr_4$ crystals at a heating rate of 10 K min^{-1}. Two strong endothermic peaks at 370 and 476 K and a weak peak at 430 K were observed (Fig. 5). A very small peak was also observed at 250 K. The phase transition temperatures were defined as T_{C1} = 370 K and T_{C2} = 430 K; 476 K was defined as the melting temperature, T_m. An analysis of the lattice parameters indicated that the peak at 250 K was independent of the phase transition temperature. According to the result previously reported by Ishiha and Horiuchi,[31] $[NH_3(CH_2)_6NH_3]ZnBr_4$ undergoes structural phase transitions at 389 and 424 K, whereas no phase transition was observed below room temperature. The T_m was reported to be 475 K. The phase transition temperatures obtained in this study were 370 and 430 K, which were slightly different from the previously reported results,[31] however, the T_m was remarkably similar. The slight differences in phase transition temperatures may vary depending on the heating rate in the DSC experiment and may also show some differences depending on the growth conditions of the crystal.

To further confirm the phase transitions, powder XRD patterns of the $[NH_3(CH_2)_6NH_3]ZnBr_4$ crystals were obtained after heating; the results in the measuring range (2θ) of 5–50° are shown in Fig. 6.

The XRD pattern at 300 K (olive) was slightly different from that recorded at 380 K (red); this difference is related to T_{C1}. Further, the XRD pattern recorded at 380 K was different from those recorded at 440 K and 460 K exhibited a clear change in structure, which is attributed to T_{C2}. The phase transition temperatures shown in the XRD results are in reasonable agreement with the endothermic peaks in the DSC curves.

3.3. Thermal properties

The TGA and DTA results measured at a heating rate of 10 K min^{-1} are shown in Fig. 7. As the temperature increased, the molecular weight of the $[NH_3(CH_2)_6NH_3]ZnBr_4$ crystals decreased. The molecular weight loss began at approximately 600 K, which was defined as the partial thermal decomposition temperature, T_d, where at 5% weight loss occurred. From the total molecular weight of 503.23 mg, the residual amounts after the decomposition of HBr and 2HBr were calculated using eqn (1) and (2), respectively:[33]

$$\{[NH_2(CH_2)_6NH_2\cdot HBr]ZnBr_3 + HBr\ (g)\}/[NH_3(CH_2)_6NH_3]ZnBr_4 = 92.75\% \quad (1)$$

$$\{[NH_2(CH_2)_6NH_2]ZnBr_2 + 2HBr\ (g)\}/[NH_3(CH_2)_6NH_3]ZnBr_4 = 85.51\% \quad (2)$$

Thus, molecular weight losses of 7% and 14% were due to the decomposition of HBr and 2HBr, respectively, and the

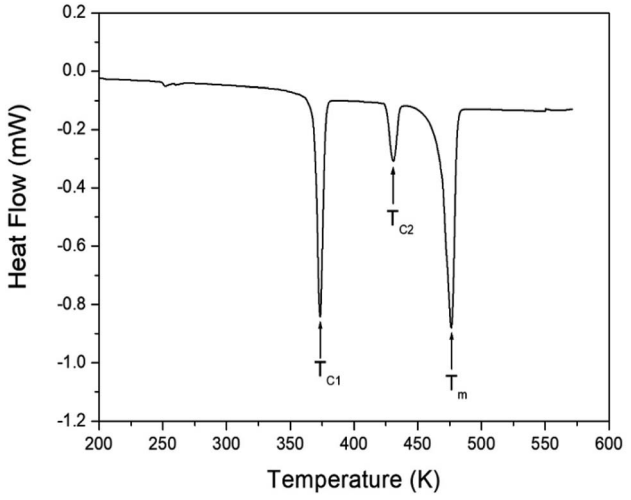

Fig. 5 DSC curve of $[NH_3(CH_2)_6NH_3]ZnBr_4$ crystal measured at heating rate of 10 K min^{-1}.

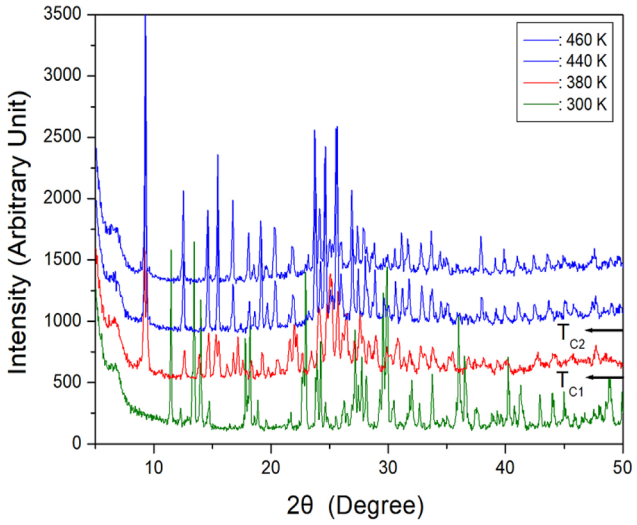

Fig. 6 Powder XRD patterns of $[NH_3(CH_2)_6NH_3]ZnBr_4$ at 300, 380, 440, and 460 K.

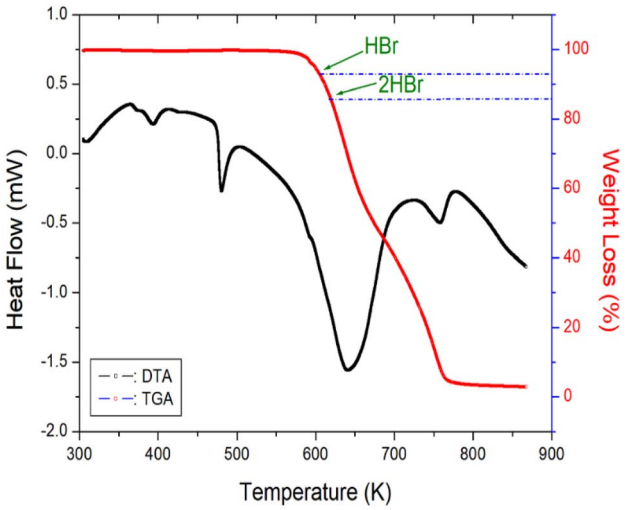

Fig. 7 TGA and DTA curves of $[NH_3(CH_2)_6NH_3]ZnBr_4$.

decomposition temperatures of HBr and 2HBr obtained by TGA were 604 and 620 K, respectively. The 55% weight loss was mainly attributed to organic decomposition. The mass rapidly decreased in the 600–750 K range, with a corresponding mass loss of 95% near 750 K. Further, the endothermic peak at 476 K, obtained from DSC, was confirmed by a polarizing microscope, which showed that the single crystal had started to melt at 470 K; thus, the endothermic peak at 476 K was denoted as the melting temperature.

3.4. ^{1}H NMR chemical shifts and spin–lattice relaxation times

Initially, the ^{1}H NMR chemical shifts of the $[NH_3(CH_2)_6NH_3]ZnBr_4$ crystals with spinning speeds of 5 and 10 kHz at 300 K were measured (ESI 1†). However, the chemical shifts measured at the two different spinning rates were observed at the same position; thus, NMR chemical shifts with respect to temperature change were measured at 5 kHz only. The *in situ* ^{1}H chemical shifts according to temperature change are shown in Fig. 8(a), and the change in chemical shifts is shown in Fig. 8(b) for better understanding. Below 260 K, six resonance lines were observed instead of the two ^{1}H signals expected from NH_3 and CH_2. NH_3 denotes ^{1}H in NH_3, and the remaining four or five signals appeared on the right side represent ^{1}H in the six CH_2. At 300 K, the ^{1}H chemical shift for NH_3 was recorded at 7.27 ppm, and those for the CH_2 were obtained at 4.32, 3.42, 2.01, and 1.69 ppm. Two ^{1}H chemical shifts at approximately 4.5–5.5 ppm overlap into one signal at 260 K; in addition, two ^{1}H chemical shifts near 3.5 ppm overlap into one signal at 400 K. Below T_{C1}, one ^{1}H peak was observed for H around C3 at the center of cation as shown in the structure in Fig. 3, and four ^{1}H peaks were observed for H around C2 and C1 with different surrounding environments. However, above T_{C1}, the symmetry around ^{1}H improved such that one ^{1}H peak was observed for each of C1, C2, and C3. The ^{1}H chemical shifts for NH_3 are continuous regardless of T_{C1}, as expressed by the different colors in each phase (Fig. 8(a)), while those for CH_2 show a slight change near T_{C1}.

The ^{1}H MAS NMR spectra were measured by changing the delay time at each temperature, and the plots of spectral intensity as a function of delay times were expressed as mono-exponential curves.

The recovery traces of the magnetization were characterized by the spin–lattice relaxation time, $T_{1\rho}$, according to eqn (3):[29,34–36]

$$I_H(\tau) = I_H(0)\exp(-\tau/T_{1\rho}) \quad (3)$$

where $I_H(\tau)$ and $I_H(0)$ are the signal intensities for the protons at time τ and $\tau = 0$, respectively. The ^{1}H $T_{1\rho}$ values were determined for NH_3 and CH_2 from eqn (3); the ^{1}H $T_{1\rho}$ results as a function of inverse temperature are shown in Fig. 9. The ^{1}H $T_{1\rho}$ values were strongly dependent on temperature change, in the order of 40–450 ms. As the temperature increased, the ^{1}H $T_{1\rho}$ values of NH_3 rapidly increased from 35 ms at 180 K to 254 ms at 320 K. Near T_{C1}, $T_{1\rho}$ shows a continuous change, similar

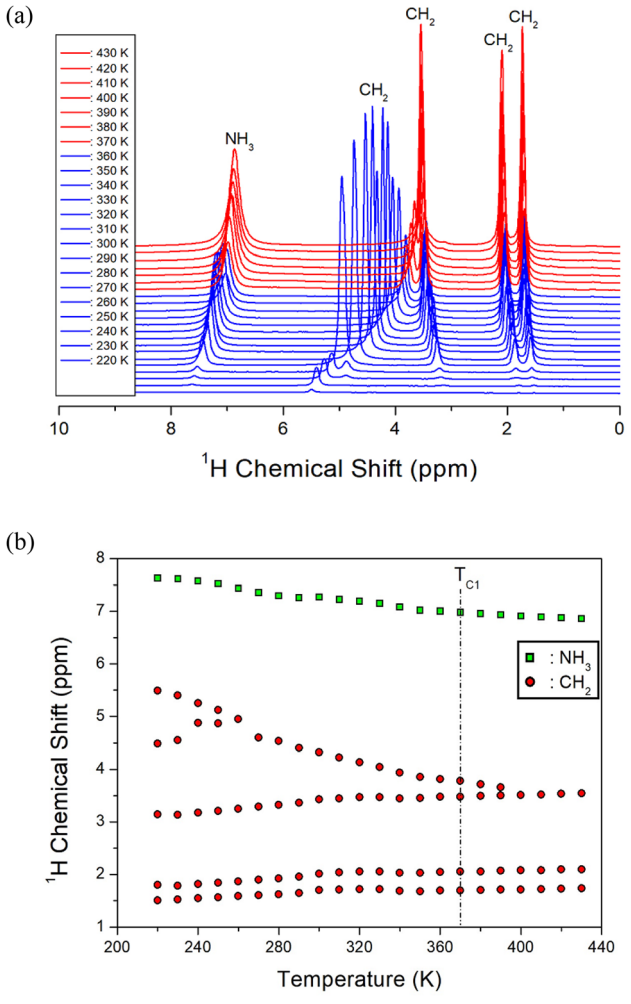

Fig. 8 (a) *In situ* ^{1}H MAS NMR spectra of NH_3 and CH_2 in $[NH_3(CH_2)_6NH_3]ZnBr_4$ according to the temperature change. (b) ^{1}H MAS NMR chemical shifts of NH_3 and CH_2 in $[NH_3(CH_2)_6NH_3]ZnBr_4$ according to the temperature change.

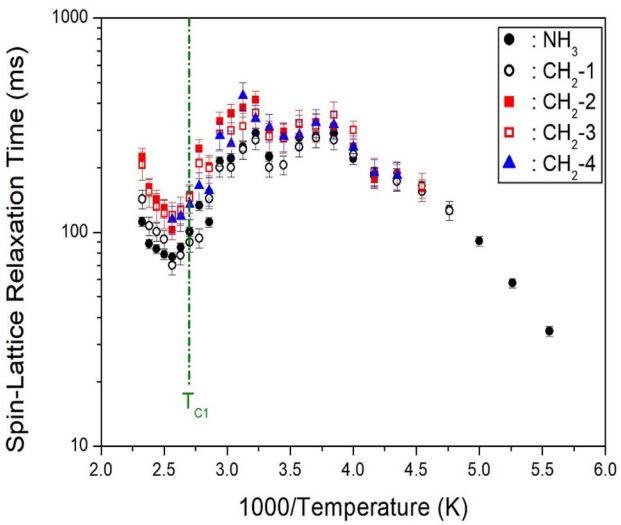

Fig. 9 ^{1}H NMR spin–lattice relaxation times of NH_3 and CH_2 in $[NH_3(CH_2)_6NH_3]ZnBr_4$ as a function of inverse temperature.

to the change in the ^{1}H chemical shift near T_{C1}. Moreover, $T_{1\rho}$ follows the trend of the Bloembergen–Purcell–Pound (BPP) phenomenon, indicating molecular motion above 320 K. The ^{1}H $T_{1\rho}$ values for CH_2 showed a similar trend to that of the ^{1}H values for NH_3.

3.5. ^{13}C NMR chemical shifts and spin–lattice relaxation times

The ^{13}C chemical shifts in the MAS NMR spectra with respect to increasing temperature are shown in Fig. 10. The ^{13}C chemical shift for TMS at 300 K was recorded at 38.3 ppm, and this value was set as the standard reference. In the $[NH_3(CH_2)_6NH_3]$ cation structure (inset of Fig. 10), CH_2 close to NH_3 at both ends of the cation was labeled C1, CH_2 at the center of the six CH_2 chains was labeled C3, and CH_2 between C3 and C1 was labeled C2. From 180 to 350 K, the chemical shifts showed a slight change with temperature, while those near T_{C1} abruptly changed. At 300 K, the ^{13}C chemical shifts were, 41.69 and 39.86, 29.55 and 27.56, and 24.94 and 20.50 ppm for C1, C2, and C3, respectively. The ^{13}C chemical shifts at 360 K were recorded at 42.48 and 41.36 ppm for C1, 27.93 and 27.00 ppm for C2, and 26.01 ppm for C3. All ^{13}C chemical shifts for C1, C2, and C3 in the cation rapidly changed near T_{C1}, indicating that the structural environment around ^{13}C changed near T_{C1}. The ^{13}C peaks corresponding to the chemical shifts for C1, C2, and C3 (Fig. 10) below T_{C1}, including those on the opposite side of C3 at the center of cation, were observed far away from each other. In contrast, the ^{13}C peaks for C1, C2, and C3 above T_{C1} were found to be close to each other. This result implies that the symmetry of the environment around C1, C2, and C3 above T_{C1} is improved as indicated by the ^{1}H chemical shifts.

The ^{13}C MAS NMR spectra measured the change in the intensities with increasing delay time at a spinning rate of 5 kHz at each temperature. The recovery traces of the ^{13}C nuclei for the delay times ranging from 0.1 to 70 ms at 300 K are represented in the inset of Fig. 11. All decay curves for C1, C2, and C3 were described by a mono-exponential function, and the ^{13}C $T_{1\rho}$ values from the slopes of their recovery traces were obtained as a function of 1000/T (Fig. 11). The ^{13}C $T_{1\rho}$ values rapidly decreased with increasing temperature, while the values near T_{C1} increased 10 times in 5 ms, similar to the rapid change in the ^{13}C chemical shifts. Here, the $T_{1\rho}$ values for C1, C2, and C3 were similar within the error range.

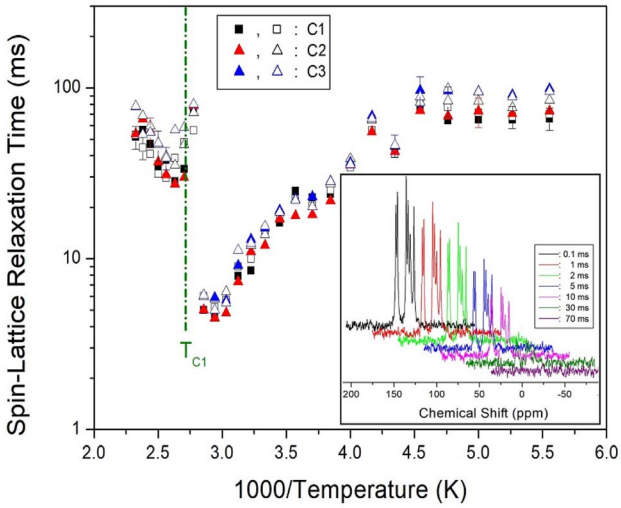

Fig. 11 ^{13}C NMR spin–lattice relaxation times of C1, C2, and C3 in $[NH_3(CH_2)_6NH_3]ZnBr_4$ as a function of inverse temperature (inset: the ^{13}C recovery traces according to the delay times between 0.1 and 70 ms at 300 K).

3.6. Static ^{14}N resonance frequency

The static NMR spectra for ^{14}N at both ends of the cation in the $[NH_3(CH_2)_6NH_3]ZnBr_4$ single crystals are shown inset of Fig. 12 (circled in red). The spectra in the temperature range of 180–400 K were obtained, and the direction of the applied magnetic field

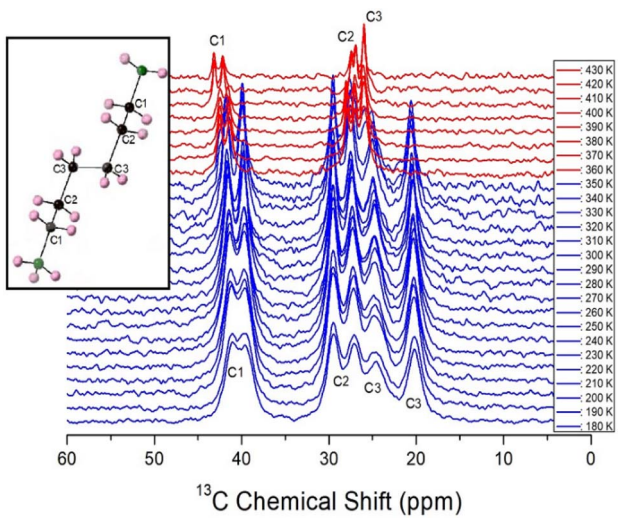

Fig. 10 *In situ* ^{13}C MAS NMR spectra of $[NH_3(CH_2)_6NH_3]ZnBr_4$ at several temperatures (inset: structure of cation).

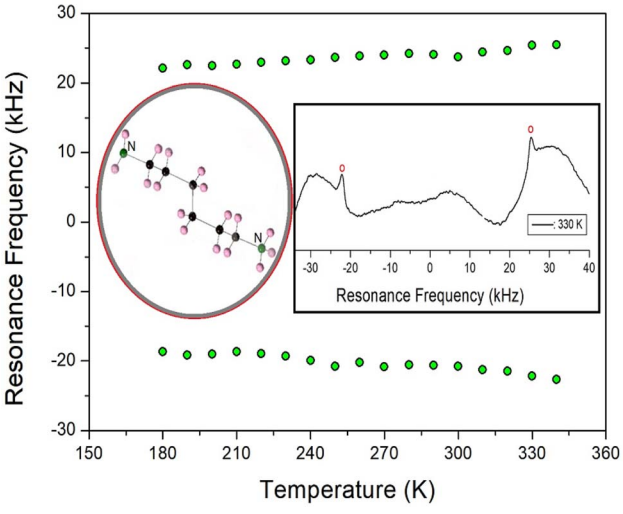

Fig. 12 ^{14}N resonance frequency of $[NH_3(CH_2)_6NH_3]ZnBr_4$ as a function of temperature (inset: structure of cation, the ^{14}N NMR spectrum at 330 K).

was measured with respect to the arbitrary direction of the single crystal. ^{14}N has a spin number of 1, and two resonance signals are expected by the quadrupole interaction.[33] The ^{14}N resonance frequency was very low at 28.90 MHz, and it was not easy to obtain a resonance signal by wiggling of the base line. However, because the intensity was small and the line width was relatively broad, it was difficult to distinguish the signals (inset of Fig. 12). The resonance frequencies for the ^{14}N NMR spectra are shown in Fig. 12 at several temperatures. It can be seen that two resonance lines slightly increased with increasing temperature. The same pairs for ^{14}N are indicated by symbols of the same color. However, the ^{14}N signals were difficult to observe at temperatures above 350 K. In the vicinity of T_{C1}, the line width of the ^{14}N signal rapidly widened, making it difficult to detect. The continuous change in the ^{14}N resonance frequency with temperature change indicated a change in the coordination geometry of the environment around N, implying a change in the quadrupole coupling constant, e^2qQ/h.

4. Conclusions

The crystal structures, phase transitions, structural geometries, thermal stabilities, and molecular dynamics of the $[NH_3(CH_2)_6NH_3]ZnBr_4$ crystals were investigated through XRD, DSC, TGA, and NMR experiments. It was discovered that the crystals belong to a monoclinic system with a $P2_1/c$ space group at 300 K, and the lattice constants are $a = 7.7833$ Å, $b = 14.5312$ Å, $c = 13.2396$ Å, $\beta = 90.8650^\circ$, and $Z = 4$. The crystals undergo two phase transitions, at 370 K (T_{C1}) and 430 K (T_{C2}), as determined by their powder XRD patterns. Our results showed that the thermal property is stable, with a thermal decomposition temperature of approximately 600 K. In the NMR spectra, the changes in the ^{1}H and ^{13}C chemical shifts were observed near T_{C1}, indicating that the structural environment around ^{1}H and ^{13}C changed. This further suggests that the energy transfer above T_{C1} is very large, indicated by the large thermal displacement around the ^{13}C atoms. The influence of ^{1}H, ^{14}N, and C1 located close to NH_3 in the $[NH_3(CH_2)_6NH_3]ZnBr_4$ crystals was not significant, indicating a minor change in the N–H···Br hydrogen bond related to the coordination geometry of the $ZnBr_4$ anion.

This material is lead-free, environmentally friendly, and stable at relatively high temperature; therefore, it is potentially applicable in solar cells.

Author contributions

A. R. Lim performed NMR experiments and wrote the manuscript. H. Ju performed XRD experiment.

Conflicts of interest

There are no conflicts to declare.

Acknowledgements

This research was supported by the Basic Science Research Program through the National Research Foundation of Korea (NRF), funded by the Ministry of Education, Science, and Technology (2018R1D1A1B07041593 and 2016R1A6A1A03012069).

References

1 O. Knop, R. E. Wasylishen, M. A. White, T. S. Cameron and M. J. M. Van Oort, *Can. J. Chem.*, 1990, **68**, 412.
2 Q. Chen, N. D. Marco, Y. Yang, T.-B. Song, C.-C. Chen, H. Zhao, Z. Hong, H. Zhou and Y. Yang, *Nano Today*, 2015, **10**, 355.
3 I. M. Hermes, S. A. Bretschneider, V. W. Bergmann, D. Klasen, J. Mars, W. Tremel, F. Laquai, H.-J. Butt, M. Mezger, R. Berger, B. J. Rodriguez and S. A. L. Weber, *J. Phys. Chem.*, 2016, **120**, 5724.
4 E. Strelcov, Q. Dong, T. Li, J. Chae, Y. Shao, Y. Deng, A. Gruverman, J. Huang and A. Centrone, *Sci. Adv.*, 2017, **3**, e1602165.
5 S. K. Abdel-Aal, A. S. Abdel-Rahman, G. G. Kocher-Oberlehner, A. Ionov and R. Mozhchil, *Acta Crystallogr., Sect. A: Found. Adv.*, 2017, **70**, C1116.
6 Y. Liu, L. Collins, R. Proksch, S. Kim, B. R. Watson, B. Doughty, T. R. Calhoun, M. Ahmadi, A. V. Ievlev, S. Jesse, S. T. Retterer, A. Belianinov, K. Xiao, J. Huang, B. G. Sumpter, S. V. Kalinin, B. Hu and O. S. Ovchinnikova, *Nat. Mater.*, 2018, **17**, 1013.
7 T. Asaji, Y. Ito, J. Seliger, V. Zagar, A. Gradisek and T. Apih, *J. Phys. Chem.*, 2012, **116**, 12422.
8 T. Asaji and K. Ashitomi, *J. Phys. Chem.*, 2013, **117**, 10185.
9 M. Simenas, A. Ciupa, M. Maczka, A. Poppl and J. Banys, *J. Phys. Chem.*, 2015, **119**, 24522.
10 N. Abhyankar, J. J. Kweon, M. Orio, S. Bertaina, M. Lee, E. S. Choi, R. Fu and N. S. Dalal, *J. Phys. Chem.*, 2017, **121**, 6314.
11 M. Simenas, S. Balciunas, M. Trzebiatowska, M. Ptak, M. Maczka, G. Volkel, A. Poppl and J. Banys, *J. Mater. Chem. C*, 2017, **5**, 4526.
12 M. Simenas, S. Balciunas, A. Ciupa, L. Vilciauskas, D. Jablonskas, M. Kinka, A. Sieradzki, V. Samulionis, M. Maczka and J. Banys, *J. Mater. Chem. C*, 2019, **7**, 6779.
13 M. Simenas, M. Ptak, A. H. Khan, L. Dagys, V. Balevicius, M. Bertmer, G. Volkel, M. Maczka, A. Poppl and J. Banys, *J. Phys. Chem.*, 2018, **122**, 10284.
14 A. H. Mahmoudkhani and V. Langer, *Acta Crystallogr., Sect. B: Struct. Sci.*, 2002, **E58**, m592.
15 Z. Cheng and J. Lin, *CrystEngComm*, 2010, **12**, 2646.
16 M. F. Mostafa and S. S. El-khiyami, *J. Solid State Chem.*, 2014, **209**, 82.
17 S. Gonzalez-Carrero, R. E. Galian and J. Perez-Prieto, *Part. Part. Syst. Charact.*, 2015, **32**, 709.
18 S. K. Abdel-Adal, G. Kocher-Oberlehner, A. Ionov and R. N. Mozhchil, *Appl. Phys. A*, 2017, **123**, 531.
19 K. Pradeesh, G. S. Yadav, M. Singh and G. Vijaya Prakash, *Mater. Chem. Phys.*, 2010, **124**, 44.
20 S. Saikumar, J. J. Ahmad, G. Baumberg and G. Vijaya Prakash, *Scr. Mater.*, 2012, **67**, 834.

21 B. Staskiewicz, O. Czupinski and Z. Czapla, *J. Mol. Struct.*, 2014, **1074**, 723.
22 S. Ahmad, C. Hanmandlu, P. K. Kanaujia and G. Vijaya Prakash, *Opt. Mater. Express*, 2014, **4**, 1313.
23 Z. Czapla, J. Przeslawski, M. Crofton, J. Janczak, O. Czupinski, A. Ingram and M. Kostrzewa, *Phase Transitions*, 2017, **90**, 637.
24 H.-Y. Zhang, Z. Wei, P.-F. Li, Y.-Y. tang, W.-Q. Liao, H.-Y. Ye, H. Cai and R.-G. Xiong, *Angew. Chem., Int. Ed.*, 2018, **57**, 526.
25 W. Zang and R.-G. Xiong, *Chem. Rev.*, 2012, **112**, 1163.
26 A. R. Lim and S. H. Kim, *ACS Omega*, 2021, **6**, 27568.
27 W. Liu, J. Xing, J. Zhao, X. Wen, K. Wang, L. Peixiang and Q. Xiong, *Adv. Opt. Mater.*, 2017, **5**, 1601045.
28 J.-C. Bissey, N. Filloleau, N.-B. Chanh, R. Berger and S. Flandrois, *Solid State Commun.*, 1998, **106**, 385.
29 A. R. Lim, S. H. Kim and Y. L. Joo, *Sci. Rep.*, 2021, **11**, 8408.
30 R. Kind, S. Plesko, P. Gunter, J. Roos and J. Fousek, *Phys. Rev. B*, 1981, **23**, 5301.
31 H. Ishiha and K. Horiuchi, *Hyperfine Interact.*, 2004, **159**, 149.
32 *SHELXTL v 6.10*, Bruker AXS, Inc., Madison, Wisconsin, USA, 2000.
33 A. R. Lim, *Sci. Rep.*, 2020, **10**, 20853.
34 A. Abragam, *The Principles of Nuclear Magnetism*, Oxford Univ. press, 1961.
35 R. K. Harris, *Nuclear Magnetic Resonance Spectroscopy*, Pitman Pub., UK, 1983.
36 J. L. Koenig, *Spectroscopy of Polymers*, Elsevier, New York, 1999.